Raman fingerprint of stacking order in HfS_2-$Ca(OH)_2$ heterobilayer

M. Yagmurcukardes,[1,*] S. Ozen,[2] F. Iyikanat,[3] F. M. Peeters,[1] and H. Sahin[2,4]
[1]*Department of Physics, University of Antwerp, Groenenborgerlaan 171, B-2020 Antwerp, Belgium*
[2]*Department of Photonics, Izmir Institute of Technology, 35430 Izmir, Turkey*
[3]*Department of Physics, Izmir Institute of Technology, 35430 Izmir, Turkey*
[4]*ICTP-ECAR Eurasian Center for Advanced Research, Izmir Institute of Technology, 35430 Izmir, Turkey*

(Received 18 January 2019; revised manuscript received 27 February 2019; published 6 May 2019)

Using density functional theory-based first-principles calculations, we investigate the stacking order dependence of the electronic and vibrational properties of HfS_2-$Ca(OH)_2$ heterobilayer structures. It is shown that while the different stacking types exhibit similar electronic and optical properties, they are distinguishable from each other in terms of their vibrational properties. Our findings on the vibrational properties are the following: (i) from the interlayer shear (SM) and layer breathing (LBM) modes we are able to deduce the AB′ stacking order, (ii) in addition, the AB′ stacking type can also be identified via the phonon softening of E_g^{I} and A_g^{III} modes which harden in the other two stacking types, and (iii) importantly, the ultrahigh frequency regime possesses distinctive properties from which we can distinguish between all stacking types. Moreover, the differences in optical and vibrational properties of various stacking types are driven by two physical effects, induced biaxial strain on the layers and the layer-layer interaction. Our results reveal that with both the phonon frequencies and corresponding activities, the Raman spectrum possesses distinctive properties for monitoring the stacking type in novel vertical heterostructures constructed by alkaline-earth-metal hydroxides.

DOI: 10.1103/PhysRevB.99.205405

I. INTRODUCTION

Interest in two-dimensional (2D) ultrathin materials has grown exponentially across materials science thanks to the successful isolation of graphene [1,2]. Beyond graphene, other novel 2D monolayer materials, such as monoatomic crystals of silicon and germanium [3–7], transition-metal dichalcogenides (TMDs) [8–11], and alkaline-earth-metal hydroxides (AEMHs) [12–15] have been added to the library of 2D materials.

Among 2D ultrathin materials, TMDs are an emerging class of materials with electronic properties ranging from metallic to semiconducting and even to superconducting which offer a wide range of opportunities for various applications [11,16]. As a member of group IVB TMDs, hafnium disulfide (HfS_2) has been predicted to possess higher carrier mobility and higher tunneling current density than those of Mo- and W-dichalcogenides [17,18]. The successful fabrication of few-layer HfS_2 field effect transistors (FETs) and observation of the high drain current and mobility have been recently reported [19,20]. Very recently, Fu *et al.* reported the synthesis of high-quality atomic layered HfS_2 crystals exhibiting ultrahigh responsivity (9 orders of magnitude higher than that of MoS_2) which is useful for ultrasensitive near-infrared phototransistors [21]. On the other hand, the bulk form of AEMHs is reported to be structurally and electronically sensitive to external physical effects such as temperature and pressure [22–28]. Aierken *et al.* investigated the thickness-dependent electronic and vibrational properties of $Ca(OH)_2$ and reported its robust direct band gap insulating character with changing thickness [12]. We also investigated the optical properties of a heterobilayer structure of monolayer $Ca(OH)_2$ combined with GaS layer and reported that their heterostructure can be used as a separator for photoinduced charge carriers which are located at different layers [15].

Thanks to the weak van der Waals interaction between constituent layers, construction of the vertical heterostructures of ultrathin materials have received considerable attention [29–39]. Jin *et al.* reported that interlayer electron-phonon interaction in WSe_2-*h*BN heterostructure plays a crucial role in engineering the electrons and phonons for possible device applications [40]. Very recently, Chen *et al.* reported that electron-phonon interaction can be controlled by the symmetry of the various 2D materials used in a heterostructure constructed on top of SiO_2 [41]. Similarly, interlayer electron-phonon coupling has been investigated in twisted bilayer graphene and MoS_2 systems and its significance on the observation of Moire phonons was reported [42,43]. It was pointed out that different stacking types result in totally different properties in both layered systems and vdW heterostructures.

Previous studies have revealed that different types of layered materials possess relatively lower (i.e., ReS_2) or higher (MoS_2, graphene, *h*-BN, etc.) energy barriers between different stacking types. We reported for bilayer ReS_2 that the energy barrier between different stacking orders is negligibly small (∼8 meV) as compared to that of bilayer MoS_2 (∼240 meV) [44]. The relatively low energy barrier indicates that in experimental conditions the existence of different stacking types is possible and thus, Raman spectrum is crucial to distinguish between them [45]. On the other hand, although graphene and monolayer *h*-BN possess similar structural

*mehmet.yagmurcukardes@uantwerpen.be

properties and stacking types in their few-layer structures, the response of different stacking types to Raman spectrum have been reported to be very different [46–48]. Notably, similar arguments hold for vdW heterostructures because of the various 2D building blocks used as constituents of the heterostructure. Therefore, as a common methodology Raman spectroscopy is crucial for the determination of the stacking type in heterostructures.

In this study we investigate the response of different stacking types to the Raman spectrum in order to distinguish them from each other in HfS_2-$Ca(OH)_2$ heterostructure. Particularly, HfS_2 can be a promising candidate for 2D-based electronic and optoelectronic applications owing to its ultrahigh on/off ratio, high carrier mobility, and high tunneling current density as an alternative to other semiconducting TMDs. On the other hand, $Ca(OH)_2$ is known to be an efficient adsorbent for CO_2 capturing in energy technologies and also has been reported to be a robust insulator upon changing thickness. As an alternative to well-known 2D insulator *h*BN, monolayer $Ca(OH)_2$ can be used as encapsulating layer to improve the properties of the 2D materials. Moreover, strong surface polarizations induced by $(OH)^-$ groups may lead to the enhancement of the semiconducting nature of the constituent layer. Overall, the construction of a heterostructure composed of HfS_2-$Ca(OH)_2$ layers offers a wide range of opportunities for its application in optoelectronic devices. In this study, we aim to show how different stacking types can be monitored via a basic Raman measurement. We propose that strong O-H bond stretching displays unusual features that help researchers to clearly monitor the stacking type in HfS_2-$Ca(OH)_2$ heterostructure.

II. COMPUTATIONAL METHODOLOGY

To investigate the structural, electronic, and vibrational properties of monolayers of HfS_2, $Ca(OH)_2$, and their heterobilayer structures, density functional theory (DFT) based first-principle calculations were performed as implemented in the Vienna *ab initio* simulation package (VASP) [49]. The Perdew-Burke-Ernzerhof (PBE) [50] form of generalized gradient approximation (GGA) was adopted to describe the electron exchange and correlation. The van der Waals (vdW) correction to the GGA functional was included by using the DFT-D2 method of Grimme [51]. For the electronic band structure calculations, spin-orbit coupling (SOC) was included with the GGA and Heyd-Scuseria-Ernzerhof (HSE06) [52] screened-nonlocal-exchange functional of the generalized Kohn-Sham scheme, respectively, for more accurate band gap calculations. The charge transfer between the individual atoms in the system was determined by the Bader technique [53].

The kinetic energy cutoff for plane-wave expansion was set to 500 eV and the energy was minimized until its variation in the following steps became 10^{-8} eV. The Gaussian smearing method was employed for the total energy calculations. The width of the smearing was chosen to be 0.05 eV. Total Hellmann-Feynman forces was taken to be 10^{-7} eV/Å for the structural optimization. $24 \times 24 \times 1$ Γ centered *k*-point samplings were used in the primitive unit cells. To avoid interaction between the neighboring layers, a vacuum space of 25 Å was implemented in the calculations. For XRD simulations of the crystal structures, the wavelength of copper K-α (1.5406 Å) was considered which is commonly used in XRD experiments.

The dielectric function of the heterobilayer was calculated by using the HSE06 functional on top of SOC. Using the dielectric function, the reflectivity (R) was calculated with the following formula:

$$R(w) = \left| \frac{\sqrt{\epsilon(w)} - 1}{\sqrt{\epsilon(w)} + 1} \right|^2. \quad (1)$$

The phonon frequencies and the corresponding off-resonant Raman activities were calculated at the Γ point of the Brillouin zone (BZ) using the small displacement method. Each atom in the primitive unit cell was initially distorted by 0.01 Å and the corresponding dynamical matrix was constructed. Then, the vibrational modes were determined by a direct diagonalization of the dynamical matrix. The corresponding Raman activity of each phonon mode was obtained from the derivative of the macroscopic dielectric tensor by using the finite-difference method. The kinetic energy cutoff for plane-wave expansion was increased up to 800 eV with a *k*-point set of $24 \times 24 \times 1$ in the case of Raman calculations.

III. STRUCTURAL, ELECTRONIC, AND PHONONIC PROPERTIES OF MONOLAYERS HfS_2 AND $Ca(OH)_2$

In contrast to monolayers of Mo- and W-dichalcogenides which crystallize in 1H phase, monolayer HfS_2 crystallizes in 1T phase in its ground state. In addition, the monolayer of $Ca(OH)_2$ possesses also a 1T crystal structure including hydroxyl groups $(OH)^-$ located symmetrically with respect to the Ca atom [see Fig. 1(a)]. In the case of monolayer HfS_2, Hf atoms are sandwiched between two layers of S atoms which corresponds to the space group $P\bar{3}m2$ and D_{3d} point group. The optimized in-plane lattice parameters are $a = b = 3.63$ Å and $a = b = 3.59$ Å for HfS_2 and $Ca(OH)_2$, respectively. The Hf-S atomic bond length is 2.55 Å while that of Ca-O is 2.37 Å. In addition, the O-H bond length in $(OH)^-$ group is 0.97 Å. Moreover, the Bader charge analysis shows that in monolayer HfS_2, a Hf atom donates $\sim$1.0 e^- to a S atom while in $Ca(OH)_2$ each H atom donates 0.6 e^- to an O atom in the hydroxyl group and each O atom also receives 0.8 e^- from a Ca atom. In addition, the thermionic work function (Φ) of each monolayer, which is the amount of energy required to remove a charge carrier located at the Fermi energy to vacuum, are calculated to be 6.19 and 4.82 eV for HfS_2 and $Ca(OH)_2$, respectively (see Table I).

The electronic properties of each monolayer crystal are investigated in terms of their electronic band structures through the whole BZ. As shown in Fig. 1(b), unlike many 1H-TMDs, 1T-HfS_2 possesses an indirect semiconducting character with a band gap of 1.98 eV. The valence band maximum (VBM) and the conduction band minimum (CBM) are located at the Γ and the M high symmetry points, respectively. Moreover, due to the d orbitals of the Hf atom, the spin-orbit splitting is found to be $\sim$136 meV at the VBM which is relatively smaller than other TMDs ($\sim$180 meV in MoS_2 and $\sim$400 meV in WS_2) [54]. The symmetry-independent spin-orbit splitting

TABLE I. For the monolayer crystals HfS_2 and $Ca(OH)_2$, the optimized lattice constants $a = b$, atomic bond lengths in the crystal d_{X-Y}, energy band gaps calculated within SOC on top of GGA E_{gap}^{GGA}, HSE on top of GGA+SOC $E_{gap}^{GGA+HSE}$, location of VBM and CBM edges in the BZ, the thermionic work function Φ, in-plane and out-of-plane dielectric constants ϵ_{xx} and ϵ_{zz}, and frequencies of Raman active phonon modes.

	$a = b$ (Å)	d_{X-Y} (Å)	E_{gap}^{GGA} (eV)	$E_{gap}^{GGA+HSE}$ (eV)	VBM/CBM	Φ (eV)	ϵ_{xx}	ϵ_{zz}	E_g (cm^{-1})	A_{1g} (cm^{-1})	E_g(OH) (cm^{-1})	A_{1g}(OH) (cm^{-1})
HfS_2	3.63	2.55	1.19	1.98	Γ/M	6.19	3.09	1.23	255.3	326.4	–	–
$Ca(OH)_2$	3.59	2.34 (Ca-O) 0.97 (O-H)	3.65	5.16	Γ/Γ	4.82	1.33	1.15	360.7	345.3	234.6	3836.1

occurs on top few valence bands which are composed of the p_x and p_y orbitals of a S atom. In contrast, $1T$-$Ca(OH)_2$ is found to be a direct gap insulator with a band gap of 5.16 eV whose VBM and CBM reside at the Γ point in the BZ [see right panel of Fig. 1(b)]. The valence bands in monolayer $Ca(OH)_2$ are mainly composed of the O-p orbitals while Ca-d orbitals mostly contribute to the conduction bands. A very small spin-orbit splitting energy of 32 meV occurs at the VBM.

For the first-order off-resonant Raman spectrum, the frequencies of phonon modes are calculated at the Γ point of the BZ [see Fig. 1(c)]. Using the vibrational character of each phonon mode, the change of dielectric constants are used in order to calculate the Raman activity of each mode. Monolayer HfS_2 exhibits nine phonon branches three of which are acoustical phonons. The remaining six optical branches consist of two nondegenerate out-of-plane phonons, A_{1g} and A_{2u} at frequencies 326.4 and 320.0 cm^{-1}, respectively, and four in-plane doubly degenerate phonon modes, E_g and E_u having frequencies 255.3 and 141.0 cm^{-1}, respectively [see Fig. 1(d)]. In contrast to $1H$-TMDs, the Raman activity of A_{1g} mode is larger than that of E_g even in monolayer HfS_2. Monolayer $Ca(OH)_2$ exhibits twelve optical phonon branches two of which have very high frequencies, 3836.1 and 3837.7 cm^{-1}, arising from O-H bond stretching. As shown in Fig. 1(d), the Raman active optical mode with frequency 3836.1 cm^{-1} is attributed to the opposite out-of-plane stretching of O and H atoms in an $(OH)^-$ group while the Ca atom remains stationary. In the Raman inactive optical mode having frequency 3837.7 cm^{-1}, similarly the O and H atoms vibrate in opposite out-of-plane directions while each $(OH)^-$ group vibrates in-phase leading to the infrared activity of the phonon mode. Apart from these two high-frequency optical modes, another ten optical branches are found to have frequencies between ∼235–435 cm^{-1} which are the usual phonon modes arising from the $1T$ nature of the structure. The phonon mode having frequency 360.7 cm^{-1} is a doubly degenerate Raman active mode which is attributed to the opposite in-plane vibration of $(OH)^-$ groups against each other. The other doubly degenerate Raman active mode is calculated to have frequency 234.6 cm^{-1} which originates from the opposite in-plane vibration of O and H atoms in a $(OH)^-$ group. In addition to the in-plane Raman active modes, there is only one nondegenerate Raman active mode with frequency 345.3 cm^{-1} and it is attributed to the opposite out-of-plane vibration of each $(OH)^-$ group. It is pointed out that the Raman activities of these three phonon modes are much smaller as compared to the high frequency optical mode.

IV. $Ca(OH)_2$-HfS_2 HETEROBILAYER

For the heterostructure consisting of two layers, three different stacking orders (i.e., the most symmetric stacking orders) are considered and the corresponding layer-layer binding energies are calculated. Taking the Hf atom as a reference, three stacking types can be defined; the AA stacking (Hf atom resides on top of Ca atom), AB (Hf on top of upper $(OH)^-$), and the AB′ [Hf on top of lower $(OH)^-$] stacking orders (see Fig. 2). Structural optimizations reveal that all three stacking orders have the same lattice parameters of $a = b = 3.62$ Å which shows the same amount of induced biaxial strain. As the heterobilayer structure is constructed, monolayer HfS_2 experiences a compressive biaxial strain of 0.28% while the monolayer $Ca(OH)_2$ exhibits a tensile strain of 0.84%. Therefore, the changing electronic and phononic properties of individual layers in the heterostructure is attributed not only to the layer-layer interaction arising from different stacking orders but also to the induced biaxial strains on each layer. As listed in Table II, the layer-layer binding energies per primitive cell are calculated to be 172, 178, and 117 meV for AA, AB, and AB′ stacking orders, respectively. Although the AB stacking is the ground state, the binding energies of the three stacking orders are very close to each other. It is important to analyze the electronic and phononic properties of these three stacking orders in order to understand the physical mechanisms driving the differences between them.

The x-ray diffraction patterns of AA, AB, and AB′ stacking orders are calculated and the distinctive parts are presented in Fig. 2(d) which allow us to identify the type of stacking. In the low-angle regime (between 2θ 7° and 14°), the XRD patterns of all stacking exhibit three peaks whose relative intensities are different. It is seen that the intensity of the

TABLE II. For the HfS_2-$Ca(OH)_2$ heterobilayer structures; the stacking configuration, the optimized lattice constants $a = b$, optimized out-of-plane layer-layer distance d_{LL}, layer-layer binding energy per primitive unit cell E_{bind}, energy band gaps calculated within SOC on top of GGA E_{gap}^{GGA}, HSE on top of GGA+SOC $E_{gap}^{GGA+HSE}$, and location of VBM and CBM edges in the BZ.

	$a = b$ (Å)	d_{LL} (Å)	E_{bind} (meV)	E_{gap}^{GGA} (eV)	$E_{gap}^{GGA+HSE}$ (eV)	VBM/CBM
AA	3.62	1.88	172	0.14	1.36	Γ/M
AB	3.62	1.89	178	0.20	1.32	Γ/M
AB′	3.62	2.55	117	0.03	0.95	Γ/M

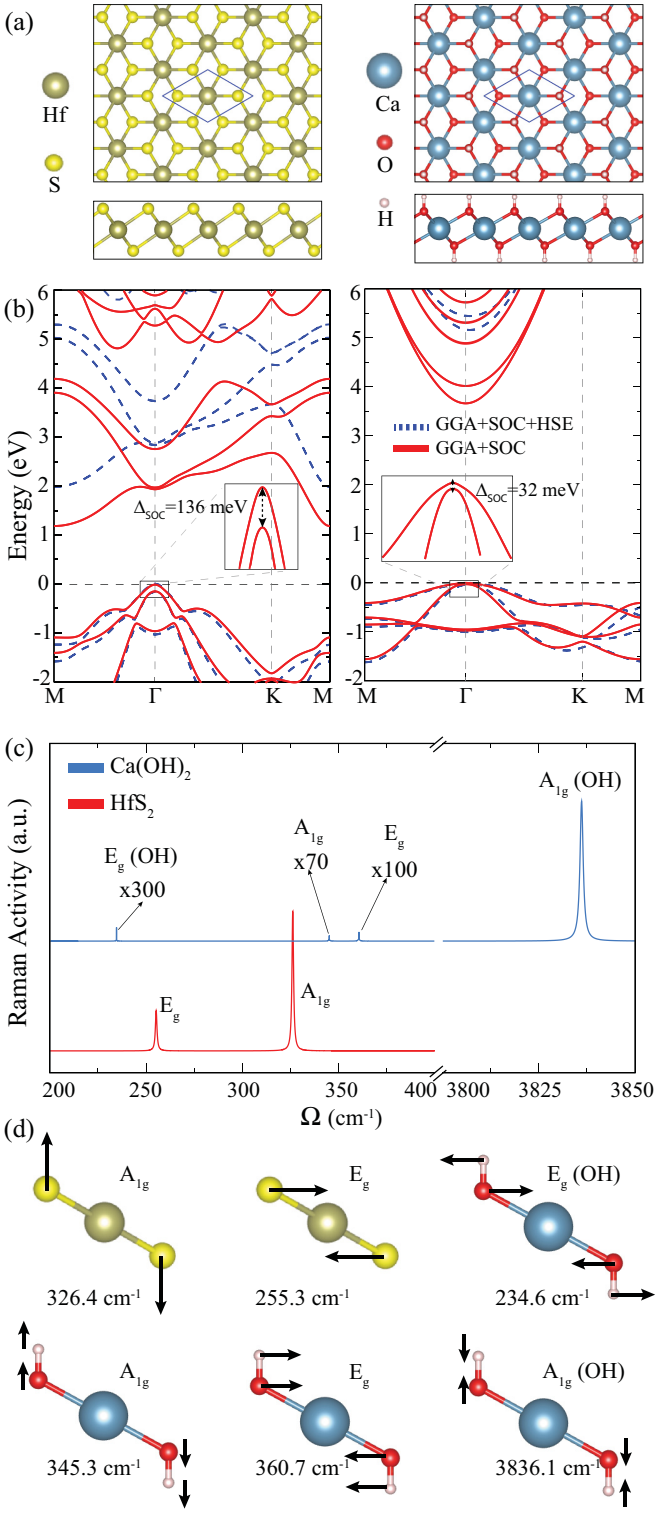

FIG. 1. For the monolayers of HfS_2 (left panel) and $Ca(OH)_2$ (right panel), (a) top and side views of the crystal structure (the blue parallelograms show the primitive unit cell of each structure) and (b) electronic band dispersions. In the electronic band dispersions, the insets display the spin-orbit splitting at the valence band maximum. The Fermi level is set to zero. (c) The calculated Raman spectra and (d) vibrational characteristic of each Raman active phonon mode.

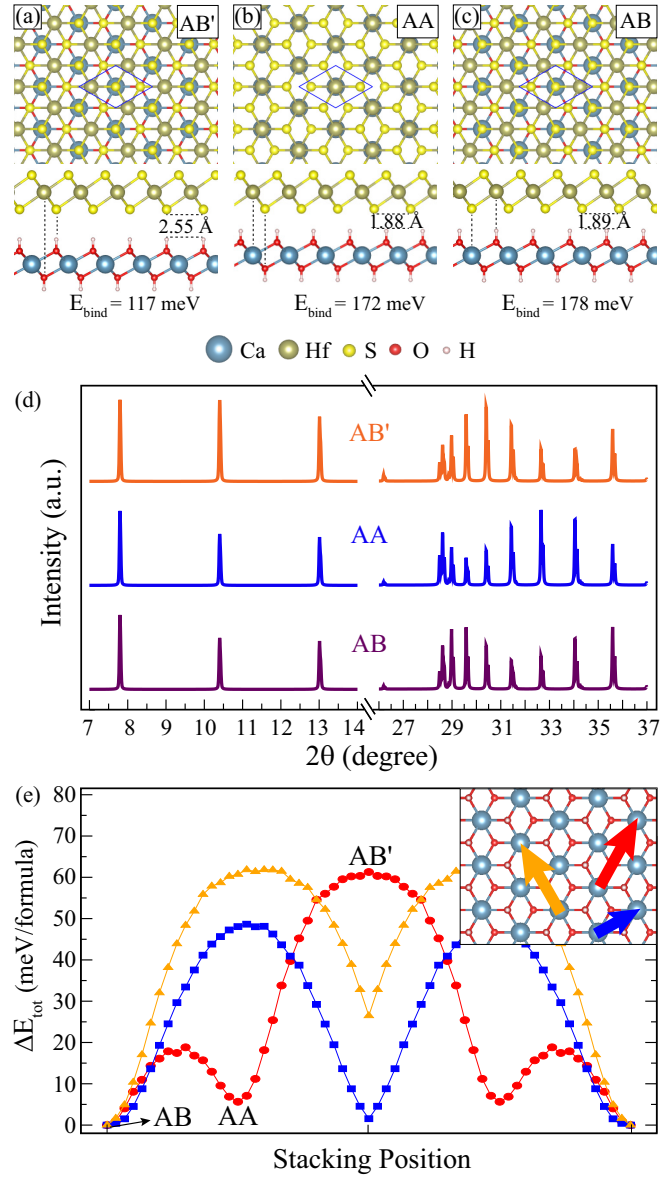

FIG. 2. Top and side views of (a) AB′, (b) AA, and (c) AB stacking configurations. (d) The calculated x-ray diffractograms of the three stacking configurations. Only the distinctive regime of the diffractograms are shown. (e) The variation of the total energy per unit cell of heterobilayer structure with respect to the sliding of HfS_2 layer on top of $Ca(OH)_2$ along three main directions. The inset shows the sliding directions.

peak around 10.5° is maximum for AB′ stacking. Moreover, between the 26° and 37° there are many peaks which are key to determine the stacking type. The intensity of the peak at 2θ 35.6° is the maximum for AB stacking order while the intensities of the peaks at 32.6° and 34° are maximum for AA stacking order. Furthermore, the peak at 2θ 31.5° has approximately the same intensity for AA and AB′ stacking while it is minimum for AB stacking. It appears that XRD patterns provide an effective way to distinguish the stacking type of HfS_2-$Ca(OH)_2$ heterobilayer.

In addition, we also analyze the energy barrier which is seen by HfS_2 layer as it slides on top of the $Ca(OH)_2$ layer.

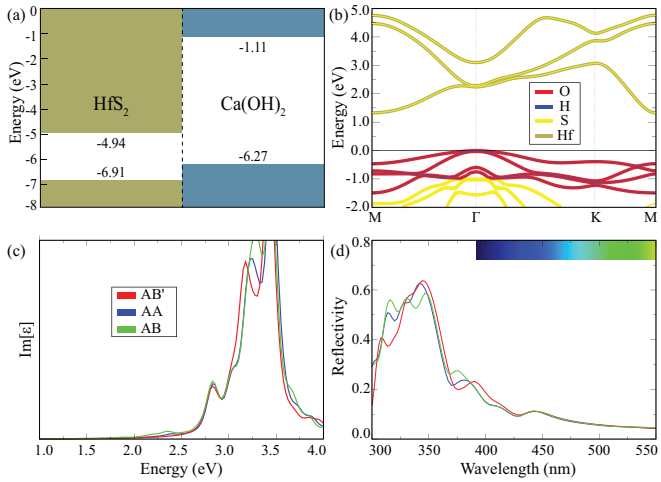

FIG. 3. (a) The band alignment between monolayers HfS_2 and $Ca(OH)_2$. (b) The electronic band dispersions of the ground state stacking in heterobilayer structure. The Fermi level is set to zero. For the three different stacking configurations: (c) the imaginary part of dielectric function and (d) reflectivity. Visible light region is presented in the inset.

In order to calculate such an energy barrier, we consider three main directions as shown in the inset of Fig. 2(e). When the HfS_2 layer slides along the direction denoted by the red curve, all three stacking orders are recovered. For the considered directions, the maximum energy barrier is calculated to be 61 meV which is much smaller than that of in bilayer TMDs (∼240 meV for MoS_2) [44]. Such a smaller energy barrier was also reported for bilayer 1*T* phase of TMDs [55]. Notice that the energy barrier between AA and AB stacking (∼20 meV) is smaller than the thermal energy at room temperature (25.7 meV). In addition, the transition to AB′ stacking can also be achieved by external effects such as increasing the temperature. Since our results reveal that different stacking orders can be formed during the experimental procedure, identification of electronic, optical, and vibrational characteristics of different stackings of HfS_2-$Ca(OH)_2$ heterobilayer is of importance.

V. MONITORING THE STACKING VIA ELECTRONIC AND OPTICAL PROPERTIES

The band alignment of the two monolayer crystals is figured out by setting the vacuum energy of each monolayer to 0 eV. It is found that the two monolayers form a type-II (staggered type) heterostructure in which the two band edges originate from different individual layers and consequently the excited electrons and holes are confined in different layers [see Fig. 3(a)], which form interlayer excitons due to the Coulomb attraction. Such a spatial separation of electrons and holes in interlayer excitons leads to longer lifetimes (in the nanosecond range) [56] than intralayer excitons (a few picoseconds) [57] that have potential for applications in optoelectronics and photovoltaics.

As shown in Fig. 3(b), for the ground state stacking order, AB stacking, the GGA+HSE calculated indirect band gap is found to be 1.32 eV whose VBM resides at the Γ point while the CBM is located at the *M* point. Due to weak vdW interaction between individual layers, there is no hybridization between the layers and therefore, the main contribution to the VBM comes from the $Ca(OH)_2$ layer while the states in the vicinity of CBM are from the HfS_2 layer. As listed in Table I, while the band gap of AA stacking order is very similar to that of AB stacking, the calculated band gap of AB′ stacking is lower since the direct interaction between the layers occur through the lower S atom and upper $(OH)^-$ which contribute to the CBM or VBM.

As presented in Figs. 3(c) and 3(d), the optical properties of the AA, AB, and AB′ stacking orders are investigated in terms of the imaginary dielectric function and reflectivity, respectively. It is seen that the overall trend for the three stacking configurations are very similar with only small differences. The first peak in the imaginary dielectric function of AA, AB, and AB′ stackings occurs between 2.0 and 2.5 eV, whereas their main peaks reside in the vicinity of 2.8 eV. In order to see visible region optical activity, we plot the reflectivity of the heterobilayer [see Fig. 3(d)]. It is seen that the optical reflectivity values are very similar in the visible range. Although it exhibits moderate reflectivity in the 300–400 nm range, the overall reflectivity in the visible region is low. Therefore, the identification of the stacking type in HfS_2-$Ca(OH)_2$ heterobilayer structure is almost impossible from an analysis of the electronic and optical properties.

VI. MONITORING THE STACKING VIA RAMAN SPECTRUM

Different stacking orders in a layered material or in a vertical heterostructure may exhibit distinctive properties in the Raman spectrum. In a Raman experiment, it is possible to distinguish different stacking orders via both the frequency shift of the phonon modes and the change in the corresponding Raman activities. In this section, we present our results on the first-order off-resonant Raman spectrum for three stacking orders

As shown at the bottom panel of Fig. 4, in addition to four characteristic Raman active modes (labeled from I to IV), one nondegenerate out-of-plane and doubly degenerate in-plane phonon modes occur in the low-frequency regime. The SM and layer breathing modes LBM are attributed to the rigid in-plane and out-of-plane vibrations of HfS_2 and $Ca(OH)_2$ layers against each other. Previously it was reported by us that the SM and LBM phonon modes are important to understand the layer-layer interaction and thus the stacking type in a layered material [58]. For the AB′ stacking configuration, the frequencies of SM and LBM are calculated to be the smallest (8.5 and 36.2 cm^{-1}, respectively) which are consequence of the low binding energy of the layers in the AB′ stacking. However, in AA and AB stacking orders the SM and LBM modes are found to be at higher frequencies (26.0–46.5 cm^{-1} and 26.7–49.2 cm^{-1} for AA and AB stacking orders, respectively). Therefore, the AB′ stacking type can be monitored via the peak frequencies of SM and LBM modes. Moreover, distinguishing between AA and AB stacking types seems to be feasible through LBM modes with the frequency difference of 2.7 cm^{-1} which is sufficiently large to be detected experimentally. Notably, the peak intensities

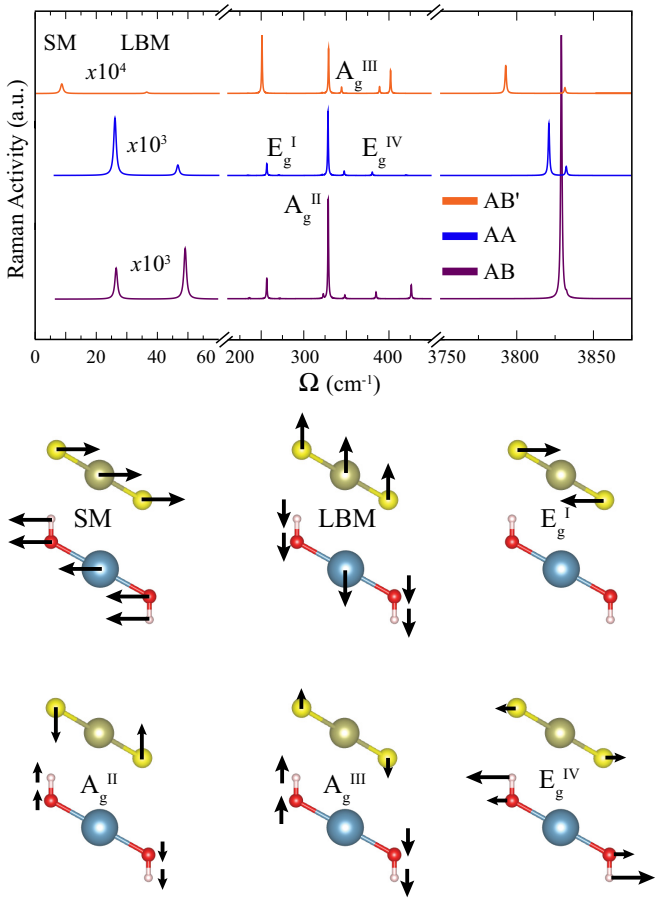

FIG. 4. Raman spectrum (top figure) and Raman active modes (bottom figure) of AB′, AA, and AB stackings.

of the low-frequency modes are too small as compared to other prominent peaks. Therefore, peak intensities are not considered to be distinctive parameters for distinguishing the stacking type even in experiments due to the dominant Rayleigh scattering intensity at zero frequency shift.

Apart from the SM and LBM modes, there are four main Raman peaks found in between ∼250–400 cm^{-1} as shown in Fig. 4. We label the in-plane phonon modes as E_g^{I}, E_g^{IV} and the out-of-plane modes as A_g^{II}, A_g^{III}. The E_g^{I} mode arises from HfS_2 layer and it displays a phonon hardening in AA and AB stacking orders (256.6 cm^{-1} in each stacking type) while it displays a phonon softening in AB′ stacking type (251.0 cm^{-1}). It is clear that AB′ stacking can be monitored via the frequency of the E_g^{I} phonon mode. In contrast to AA and AB stacking types, in AB′ stacking the frequency shift of the E_g^{I} mode is dominated by the layer-layer interaction over the induced strain. Another in-plane Raman active mode E_g^{IV} arises from the opposite vibrations of $(OH)^-$ against each other. It is originally the E_g mode of monolayer $Ca(OH)_2$ and it is coupled with that of the HfS_2 layer in the heterobilayer structure. The frequency of the E_g^{IV} mode is calculated to be 380.4, 384.9, and 388.9 cm^{-1} in AA, AB, and AB′ stacking types, respectively. It is seen that the frequency differences between the three stacking types are considerable and are sufficiently large in order to be used to monitor the type of stacking.

The other two Raman active modes, labeled as A_g^{II} and A_g^{III}, are attributed to the out-of-plane vibration of the atoms from different layers. The A_g^{II} mode is a coupled out-of-plane mode in which the main contribution arises from the HfS_2 layer. Contrarily, in the A_g^{III} mode the main contribution to the vibration arises from the $Ca(OH)_2$ layer. The frequencies of the A_g^{II} mode are calculated to be 328.4, 328.7, and 329.1 cm^{-1} in AA, AB, and AB′ stacking types, respectively. It is obvious that the A_g^{II} mode displays phonon hardening in all stacking types as compared to monolayer HfS_2. Due to the same frequency shift behavior and small frequency differences, monitoring of the stacking type via the A_g^{II} mode is not feasible. However, the A_g^{III} mode exhibits phonon hardening in AA and AB stacking (345.6 and 346.9 cm^{-1}, respectively) and it displays phonon softening in AB′ stacking (344.4 cm^{-1}) as compared to its frequency in $Ca(OH)_2$ layer (345.3 cm^{-1}). Although there are small frequency differences of A_g^{III} mode between various stackings, its phonon softening in AB′ stacking can be used to distinguish the stacking order.

There are two Raman active modes having high frequencies that arise from the O-H bond stretching. In addition, an additional Raman active phonon mode appears in the heterobilayer structure that is attributed to the opposite out-of-plane vibration of O-H atoms in a $(OH)^-$ group while each $(OH)^-$ also vibrates out-of-phase. Both of the O-H stretching modes display phonon softening as compared to their frequencies in monolayer $Ca(OH)_2$. As shown in the top panel of Fig. 4, the relative frequencies of the two phonon modes can be used to monitor the type of stacking order. Frequency difference of the two modes are found to be 3.3, 11.3, and 38.6 cm^{-1} for AB, AA, and AB′ stacking configurations, respectively. It is obvious that AB stacking order can be distinguished due to the smallest frequency difference while the AB′ stacking can be monitored with its largest frequency difference. Moreover, the AB stacking can be also distinguished via the Raman activity ratio of the two modes that is calculated to be approximately 100 times greater than those for AA and AB′ stacking types. Furthermore, the AB stacking can also be identified due to the largest Raman activity of the phonon mode having frequency 3829.1 cm^{-1} (approximately one order of magnitude larger). The reason for such relatively large activity is the dominant contribution of in-plane dielectric constants to the Raman tensor. The general form of Raman tensor for out-of-plane vibrations in 2D materials is known to be totally diagonal [58]. Calculated in-plane components of the dielectric tensor are found to be slightly larger for AB stacking (2.90 for AB stacking, 2.86 and 2.80 for AA and AB′ stacking types, respectively). The variation of the in-plane dielectric constant with respect to O-H bond stretching is larger in AB stacking type. Our results reveal that the ultrahigh frequency regime of the Raman spectrum can be used to monitor the type of stacking in HfS_2-$Ca(OH)_2$ heterobilayer structure in terms of both peak frequencies and Raman activities. Moreover, our findings show that particularly the O-H bond stretchings in layered AEHMs can be used as important keys for identification of stacking type in vdW heterostructures composed of any 2D material and monolayer AEHMs.

VII. CONCLUSIONS

In this study we investigated the stacking order dependence of the electronic and vibrational properties of HfS_2-$Ca(OH)_2$ heterobilayer structures by means of the electronic band dispersions and the Raman spectra. Electronic band dispersions and optical spectrum revealed that the band gap varies very little between the different stacking types. Analysis of Raman spectra showed that different stacking types possess distinct coupling phenomena which can be used to identify the type of the stacking. Our findings on the phononic properties are the following: (i) the SM and LBM modes are able to monitor the AB′ stacking order, (ii) in addition, the AB′ stacking can be identified via the phonon softening of the E_g^{I} and A_g^{III} modes which harden in the other two stackings, and (iii) importantly, the ultrahigh frequency regime displays distinctive properties which can be used to distinguish between all stacking types. Moreover, the differences in optical and vibrational properties of various stacking types were found to be driven by two physical effects, induced biaxial strain on the layers and the layer-layer interaction. Our results reveal that from both the phonon frequencies and the corresponding Raman activities it is possible to distinguish between the different stacking types in these novel vertical heterostructures constructed by alkaline-earth-metal hydroxides.

ACKNOWLEDGMENTS

Computational resources were provided by TUBITAK ULAKBIM, High Performance and Grid Computing Center (TR-Grid e-Infrastructure). H.S. acknowledges financial support from the Scientific and Technological Research Council of Turkey (TUBITAK) under the Project No. 117F095. H.S. acknowledges support from Turkish Academy of Sciences under the GEBIP program. This work is supported by the Flemish Science Foundation (FWO-Vl) by a postdoctoral fellowship (M.Y.).

[1] S. K. Novoselov, A. K. Geim, S. V. Morozov, D. Jiang, Y. Zhang, S. V. Dubonos, I. Grigorieva, and A. A. Firsov, Science **306**, 666 (2004).
[2] K. S. Novoselov, A. K. Geim, S. V. Morozov, D. Jiang, M. I. Katsnelson, I. V. Grigorieva, S. V. Dubonos, and A. A. Firsov, Nature (London) **438**, 197 (2005).
[3] G. G. Guzmán-Verri and L. C. L. Y. Voon, Phys. Rev. B **76**, 075131 (2007).
[4] F. Bechstedt, L. Matthes, P. Gori, and O. Pulci, Appl. Phys. Lett. **100**, 261906 (2012).
[5] S. Cahangirov, M. Topsakal, E. Aktürk, H. Şahin, and S. Ciraci, Phys. Rev. Lett. **102**, 236804 (2009).
[6] M. Houssa, G. Pourtois, V. V. Afanas'ev, and A. Stesmans, Appl. Phys. Lett. **96**, 082111 (2010).
[7] H. Sahin, S. Cahangirov, M. Topsakal, E. Bekaroglu, E. Akturk, R. T. Senger, and S. Ciraci, Phys. Rev. B **80**, 155453 (2009).
[8] A. H. C. Neto and K. Novoselov, Rep. Prog. Phys. **74**, 082501 (2011).
[9] K. F. Mak, C. Lee, J. Hone, J. Shan, and T. F. Heinz, Phys. Rev. Lett. **105**, 136805 (2010).
[10] A. Splendiani, L. Sun, Y. Zhang, T. Li, J. Kim, C.-Y. Chim, G. Galli, and F. Wang, Nano Lett. **10**, 1271 (2010).
[11] B. Radisavljevic, A. Radenovic, J. Brivio, V. Giacometti, and A. Kis, Nat. Nanotechnol. **6**, 147 (2011)
[12] Y. Aierken, H. Sahin, F. İyikanat, S. Horzum, A. Suslu, B. Chen, R. T. Senger, S. Tongay, and F. M. Peeters, Phys. Rev. B **91**, 245413 (2015).
[13] A. Suslu, K. Wu, H. Sahin, B. Chen, S. Yang, H. Cai, T. Aoki, S. Horzum, J. Kang, F. M. Peeters, and S. Tongay, Sci. Rep. **6**, 20525 (2016).
[14] M. Yagmurcukardes, E. Torun, R. T. Senger, F. M. Peeters, and H. Sahin, Phys. Rev. B **94**, 195403 (2016)
[15] E. Torun, H. Sahin, and F. M. Peeters, Phys. Rev. B **93**, 075111 (2016).
[16] J. T. Ye, Y. J. Zhang, R. Akashi, M. S. Bahramy, R. Arita, and Y. Iwasa, Science **338**, 1193 (2012).
[17] G. Fiori, F. Bonaccorso, G. Iannaccone, T. Palacios, D. Neumaier, A. Seabaugh, S. K. Banerjee, and L. Colombo, Nat. Nanotechnol. **9**, 768 (2014).
[18] Y. H. Lee, X. Q. Zhang, W. Zhang, M. T. Chang, C. T. Lin, K. D. Chang, Y. C. Yu, J. T. Wang, C. S. Chang, L. J. Li, and T. W. Lin, Adv. Mater. **24**, 2320 (2012).
[19] T. Kanazawa, T. Amemiya, and A. Ishikawa, Sci. Rep. **6**, 22277 (2016).
[20] K. Xu, Z. Wang, F. Wang, Y. Huang, F. Wang, L. Yin, C. Jiang, and J. He, Adv. Mater. **27**, 7881 (2015).
[21] L. Fu, F. Wang, B. Wu, N. Wu, W. Huang, H. Wang, C. Jin, L. Zhuang, J. He, L. Fu, and Y. Liu, Adv. Mater. **29**, 1700439 (2017).
[22] M. B. Kruger, Q. Williams, and R. Jeanloz, J. Chem. Phys. **91**, 5910 (1989).
[23] J. H. Nguyen, M. B. Kruger, and R. Jeanloz, Phys. Rev. Lett. **78**, 1936 (1997).
[24] S. Raugei, P. L. Silvestrelli, and M. Parrinello, Phys. Rev. Lett. **83**, 2222 (1999).
[25] T. S. Duffy, C. Meade, Y. Fei, H. K. Mao, and R. J. Hemley, Am. Mineral. **80**, 222 (1995).
[26] S. Ekbundit, K. Leinenweber, J. L. Yarger, J. S. Robinson, M. Verhelst-Voorhees, and G. H. Wolf, J. Solid State Chem. **126**, 300 (1996).
[27] K. Catalli, S.-H. Shim, and V. B. Prakapenka, Geophys. Res. Lett. **35**, 05312 (2008).
[28] R. Iizuka, H. Kagi, K. Komatsu, D. Ushijima, S. Nakano, A. Sano-Furukawa, T. Nagai, and T. Yagi, Phys. Chem. Miner. **38**, 777 (2011).
[29] A. K. Geim and I. V. Grigorieva, Nature (London) **499**, 419 (2013).
[30] L. Britnell, R. V. Gorbachev, R. Jalil, B. D. Belle, F. Schedin, A. Mishchenko, T. Georgiou, M. I. Katsnelson, L. Eaves, S. V. Morozov, N. M. R. Peres, J. Leist, A. K. Geim, and K. S. Novoselov, Science **335**, 947 (2012).
[31] H. Fang, C. Battaglia, C. Carraro, S. Nemsak, B. Ozdol, J. S. Kang, H. A. Bechtel, S. B. Desai, F. Kronast, A. A. Unal, G. Conti, C. Conlon, G. K. Palsson, M. C. Martin, A. M. Minor, C. S. Fadley, E. Yablonovitch, R. Maboudian, and A. Javey, Proc. Natl. Acad. Sci. USA **111**, 6198 (2014).
[32] C.-H. Lee, G.-H. Lee, A. M. van der Zande, W. Chen, Y. Li, M. Han, X. Cui, G. Arefe, C. Nuckolls, T. F. Heinz,

J. Guo, J. Hone, and P. Kim, Nat. Nanotechnol. **9**, 676 (2014).
[33] B. Hunt, J. D. Sanchez-Yamagishi, A. F. Young, M. Yankowitz, B. J. LeRoy, K. Watanabe, T. Taniguchi, P. Moon, M. Koshino, P. Jarillo-Herrero, and R. C. Ashoori, Science **340**, 1427 (2013).
[34] X. Hong, J. Kim, S.-F. Shi, Y. Zhang, C. Jin, Y. Sun, S. Tongay, J. Wu, Y. Zhang, and F. Wang, Nat. Nanotechnol. **9**, 682 (2014).
[35] A. C. Ferrari, F. Bonaccorso, V. Fal'Ko, K. S. Novoselov, S. Roche, P. Bøggild, S. Borini, F. H. L. Koppens, V. Palermo, N. Pugno *et al.*, Nanoscale **7**, 4598 (2015).
[36] C. Tan and H. Zhang, Chem. Soc. Rev. **44**, 2713 (2015).
[37] J. S. Ross, P. Klement, A. M. Jones, N. J. Ghimire, J. Yan, D. G. Mandrus, T. Taniguchi, K. Watanabe, K. Kitamura, W. Yao, D. H. Cobden, and X. Xu, Nat. Nanotechnol. **9**, 268 (2014).
[38] M. M. Furchi, A. Pospischil, F. Libisch, J. Burgdörfer, and T. Mueller, Nano Lett. **14**, 4785 (2014).
[39] E. V. Calman, C. J. Dorow, M. M. Fogler, L. V. Butov, S. Hu, A. Mishchenko, and A. K. Geim, Appl. Phys. Lett. **108**, 101901 (2016).
[40] C. Jin, J. Kim, J. Suh, Z. Shi, B. Chen, X. Fan, M. Kam, K. Watanabe, T. Taniguchi, S. Tongay, A. Zettl, J. Wu, and F. Wang, Nat. Phys. **13**, 127 (2017).
[41] C. Chen, X. Chen, H. Yu, Y. Shao, Q. Guo, B. Deng, S. Lee, C. Ma, K. Watanabe, T. Taniguchi, J.-G. Park, S. Huang, W. Yao, and F. Xia, ACS Nano **13**, 552 (2019).
[42] M.-L. Lin, Q.-H. Tan, J.-B. Wu, X.-S. Chen, J.-H. Wang, Y.-H. Pan, X. Zhang, X. Cong, J. Zhang, W. Ji, P.-A. Hu, K.-H. Liu, and P.-H. Tan, ACS Nano **12**, 8770 (2018).
[43] G. S. N. Eliel, M. V. O. Moutinho, A. C. Gadelha, A. Righi, L. C. Campos, H. B. Ribeiro, P.-W. Chiu, K. Watanabe, T. Taniguchi, P. Puech, M. Paillet, T. Michel, P. Venezuela, and M. A. Pimenta, Nat. Commun. **9**, 1221 (2018).
[44] S. Tongay, H. Sahin, C. Ko, A. Luce, W. Fan, K. Liu, J. Zhou, Y. S. Huang, C. H. Ho, J. Yan, D. F. Ogletree, S. Aloni, J. Ji, S. Li, J. Li, F. M. Peeters, and J. Wu, Nat. Commun. **5**, 3252 (2014).
[45] R. He, J.-A. Yan, Z. Yin, Z. Ye, G. Ye, J. Cheng, J. Li, and C. H. Lui, Nano Lett. **16**, 1404 (2016).
[46] C. H. Lui, Z. Li, Z. Chen, P. V. Klimov, L. E. Brus, and T. F. Heinz, Nano Lett. **11**, 164 (2011).
[47] R. Rao, R. Podila, R. Tsuchikawa, J. Katoch, D. Tishler, A. M. Rao, and M. Ishigami, ACS Nano **5**, 1 (2011).
[48] C. H. Lui, Z. Ye, C. Keiser, E. B. Barros, and R. He, Appl. Phys. Lett. **106**, 041904 (2015).
[49] G. Kresse and J. Furthmuller, Phys. Rev. B **54**, 11169 (1996).
[50] J. P. Perdew, K. Burke, and M. Ernzerhof, Phys. Rev. Lett. **77**, 3865 (1996).
[51] S. J. Grimme, J. Comput. Chem. **27**, 1787 (2006).
[52] J. Heyd, G. E. Scuseria, and M. Ernzerhof, J. Chem. Phys. **118**, 8207 (2003).
[53] G. Henkelmana, A. Arnaldssonb, and H. Jónsson, Comput. Mater. Sci. **36**, 354 (2006).
[54] D. W. Latzke, W. Zhang, A. Suslu, T.-R. Chang, H. Lin, H.-T. Jeng, S. Tongay, J. Wu, A. Bansil, and A. Lanzara, Phys. Rev. B **91**, 235202 (2015).
[55] C. Bacaksiz, S. Cahangirov, A. Rubio, R. T. Senger, F. M. Peeters, and H. Sahin, Phys. Rev. B **93**, 125403 (2016).
[56] M. Palummo, M. Bernardi, and J. C. Grossman, Nano Lett. **15**, 2794 (2015).
[57] C. Robert, D. Lagarde, F. Cadiz, G. Wang, B. Lassagne, T. Amand, A. Balocchi, P. Renucci, S. Tongay, B. Urbaszek, and X. Marie, Phys. Rev. B **93**, 205423 (2016).
[58] M. Yagmurcukardes, F. M. Peeters, and H. Sahin, Phys. Rev. B **98**, 085431 (2018).